Progress In Electromagnetics Research C, Vol. 123, 117–133, 2022

Improved Higher-Order Sliding Mode Controller for Model Predictive Current Control of PMSM

Qianghui Xiao[1], Zihao Liu[1], Yang Zhang[1, *], Zhe Li[1], Bing Luo[2], and Tingting Wang[2]

Abstract—To improve the control accuracy of the model prediction current (MPC) loop of a permanent magnet synchronous motor (PMSM), a new high-order super-twisting sliding-mode controller combined with a sliding-mode disturbance observer is proposed as a speed control strategy. Firstly, the linear term is added to the scaling term based on the original algorithm, which enhances robustness while weakening jitter. In addition, load perturbations and parameter uptake in the system are considered. The perturbation observation error is introduced into the switching gain function, and an improved sliding-mode disturbance observer is designed as feedforward compensation. The disturbance immunity of the system is effectively enhanced. Simulated and experimental results verify the correctness and effectiveness of this control strategy.

1. INTRODUCTION

Permanent magnet synchronous motor (PMSM) control techniques are continuously explored, and fast and reliable control strategies are essential [1, 2]. In addition to Vector Control (VC) and Direct Torque Control (DTC), Model Predictive Control (MPC) has been widely investigated as a control method for PMSM. Depending on the number of voltage vectors acting in a single control cycle, the MPC of PMSM is classified as single-vector, double-vector [3, 4], and triple-vector [5] model predictive current control. Single vector control is simple, but current pulsation is high. Triple-vector control can improve the system performance, but it is computationally intensive and requires high hardware requirements. Therefore, two-vector model predictive control is adopted in this paper.

However, the PMSM is a nonlinear, multi-variable, and strongly coupled controlled object, and the control system is susceptible to uncertainties such as external load disturbances and parameter uptake [6, 7]. In the speed control system of a PMSM, the traditional proportional integral (PI) controller is often used. However, it is challenging to meet high-performance control requirements due to its control sensitivity to system parameters, susceptibility to external disturbances, and low control accuracy [8]. This leads to poor control accuracy of model predictive control of the current loop.

To further improve the response speed and disturbance immunity of the system, some modern control theories such as fuzzy control, adaptive control [9], self-turbulence control [10], neural networks [11], and sliding mode control [12, 13] have been successfully applied to the speed control of PMSM. Among them, sliding mode control (SMC) is widely used because of its robustness, fast dynamic response, and easy implementation [14].

Improving the dynamic response performance of the system and weakening the jitter is the key to this paper's research. Ref. [15] proposes a higher-order sliding mode control: its algorithm comprises a proportional term and an integral term. When the point of motion reaches the sliding mode surface, the integral term moves the system trajectory around the origin to ensure the continuity of the output

Received 2 June 2022, Accepted 16 August 2022, Scheduled 26 August 2022
* Corresponding author: Yang Zhang (459387623@qq.com).
[1] Hunan University of Technology, Zhuzhou 412007, China. [2] CSG Electric Power Research Institute Co. Ltd., Guangzhou 510663, China.

control signal [16]. This weakens the jitter phenomenon, but its effect is mediocre. Ref. [17] applies super-twisting algorithm to the speed controller of a PMSM. It is compared with a sliding mode control based on the exponential convergence law. This control strategy improves the system's speed while suppressing sliding mode jitter. However, the perturbation term in the algorithm is minimally bounded.

Usually, sliding-mode control is used to improve its control performance at the cost of setting too high switching gains, which may lead to severe system jitter and even collapse [18, 19]. Therefore, [20] proposes a PMSM speed regulation system based on an adaptive over-torsion algorithm, which effectively solves the problem of excessive gain. However, due to the discontinuity of the integral term of the original algorithm, a super-twisting fractional order (STFO) controller was proposed in [21] to improve its control performance. The use of convergence methods in the convergence process has been proposed, thus effectively weakening the jitter. Ref. [22] designed a continuous and fast adaptive terminal sliding mode convergence method to achieve high accuracy tracking. However, the control scheme is difficult to implement due to its high start-up current and more complex design.

Another method is to weaken jitter and improve immunity by adding a disturbance observer. In [23], a generalized proportional-integral observation (GPIO) strategy combined with super-twisting sliding mode control is designed. This control strategy has a small switching gain factor and a high tracking accuracy. However, due to the discontinuity of its integral term, it leads to a more obvious jitter. Refs. [24, 25] compensate in real-time by introducing a disturbance observer, which improves the immunity of the control system to disturbances. However, the design of the observer relies on an accurate model of the drive system.

Since the scaling term in the super-twisting algorithm is a square root calculation [26], the above strategy still suffers from the lack of fast enough arrival time and poor immunity to disturbances of the super-twisting algorithm. Furthermore, there are problems with the value and design of the switching gain coefficients for such perturbation observers and the dependence on an accurate system model.

To sum up, this paper proposes a high-order sliding mode controller (SMC) based on a new super-twisting algorithm (NSTA) and combined with a sliding mode disturbance observer (SMDO) as a speed control strategy. Linear term is added to the scaling term of the original algorithm, effectively weakening the system's jitter. In addition, an improved SMDO is designed, taking load disturbances and parameter ingestion into account. A perturbation observation error is introduced based on the conventional switching gain function. The total disturbance of the observer output is fed back into the controller, improving disturbance immunity of the system.

2. PMSM MODEL

The simplified voltage equation for a PMSM under ideal assumptions is:

$$\begin{bmatrix} u_a \\ u_b \\ u_c \end{bmatrix} = \begin{bmatrix} R_s & 0 & 0 \\ 0 & R_s & 0 \\ 0 & 0 & R_s \end{bmatrix} \begin{bmatrix} i_a \\ i_b \\ i_c \end{bmatrix} + p \begin{bmatrix} \psi_a \\ \psi_b \\ \psi_c \end{bmatrix} \tag{1}$$

where ψ_a, ψ_b, ψ_c are the magnetic chain of the three-phase stator winding; u_a, u_b, u_c are the phase voltage instantaneous values; i_a, i_b, i_c are the phase current instantaneous values of the three-phase stator winding; R_s is the resistance of the three-phase stator winding; p is the differential operator.

Since the surface-mounted permanent magnet synchronous motor has $L_q = L_d$, the current equation in the dq coordinate system:

$$\frac{di_q}{dt} = \left(u_q - R_s i_q - \omega_{re} L_s i_d - \omega_{re}\psi_f\right)/L_s \tag{2}$$

$$\frac{di_d}{dt} = \left(u_d - R_s i_d + \omega_{re} L_s i_q\right)/L_s \tag{3}$$

where u_d is the stator direct-axis voltage component; u_q is the stator cross-axis voltage component; i_d is the current direct-axis component; i_q is the current cross-axis component; L_s is the stator inductance; ω_{re} is the rotor electric angular velocity; ψ_f is the permanent magnet magnetic chain.

The first-order Eulerian discretization of Eqs. (2) and (3) gives [27]:

$$i_q(k+1) = i_q(k) + \left[u_q(k) - R_s i_q(k) - \omega_{re} L_s i_q(k) - \omega_{re}\psi_f\right] T_s/L_s \tag{4}$$

$$i_d(k+1) = i_d(k) + \left[u_d(k) - R_s i_d(k) + L_s i_q(k)\right] T_s/L_s \tag{5}$$

where $i_d(k)$, $i_q(k)$ are the feedback values of d and q-axis currents of the stator current at the current moment; $i_d(k+1)$, $i_q(k+1)$ are the predicted values of d and q-axis currents of the stator current at the next moment, respectively; T_s is the sampling period of the system.

The equation of motion of a permanent magnet synchronous motor is expressed as:

$$\frac{dw}{dt} = \frac{3p_n\psi_f}{2}i_q - \frac{B}{J}\omega - \frac{T_L}{J} \tag{6}$$

where p_n is the polar logarithm; ω is the mechanical angular velocity; B is the viscous friction coefficient; J is the rotational inertia; and T_L is the load torque.

3. SLIPFORM SPEED CONTROLLER DESIGN

3.1. Controller Design

The higher-order sliding mode algorithm solves the conflict between arrival speed and system jitter. Unlike other higher-order sliding mode algorithms, the super-twisting algorithm does not need to derive the sliding mode surface. Thus, the sliding mode surface and its derivatives can be simultaneously stabilized to zero, avoiding the simplicity of introducing noise control. Its general expression is as follows:

$$\begin{aligned} u &= -\alpha|s|^{1/2}\text{sign}(s) + u_1 \\ \dot{u}_1 &= -\beta\text{sign}(s) + \dot{e} \end{aligned} \tag{7}$$

where s is the sliding variable; e is the perturbation term; α and β are the sliding mode gain coefficients; and the symbol sign(s) is the switching function.

The proportional term $\alpha|s|^{1/2}\text{sign}(s)$ can effectively improve the arrival speed of the algorithm; however, its sliding mode surface is calculated using the square root, and the arrival speed of the algorithm and the anti-interference ability are directly affected by the gain of the proportional term. In order to improve the anti-interference ability and arrival speed, this paper proposes a new super-twisting algorithm, namely:

$$\begin{aligned} u &= -\alpha|s|^{1/2}\text{sign}(s) - ks + u_1 \\ \dot{u}_1 &= -\beta\text{sign}(s) + \dot{e} \end{aligned} \tag{8}$$

where ks is a linear term and $k > 0$.

In this paper, the slide surface selected for the speed control loop is:

$$s = x = \omega^* - \omega \tag{9}$$

Derivation of Eq. (9) yields:

$$\dot{s} = \dot{x} = -\dot{\omega} \tag{10}$$

By comparing Eq. (6), Eq. (8), and Eq. (10), the output of this controller is obtained as follows:

$$i_q^* = \frac{2J}{3p_n\psi_f}\left(\left(\frac{B}{J}\omega + \frac{T_L}{J}\right) + \alpha|s|^{\frac{1}{2}}\text{sign}(s) + ks + e + \int \beta\text{sign}(s)\text{d}t\right) \tag{11}$$

3.2. System Stability Analysis

According to Eq. (11), when $\delta \geqslant 0$ and $2|e| \leqslant \delta$ is elected, α, β, and k satisfy the following conditions.

$$\begin{cases} \alpha > 2 \\ \beta > \dfrac{\left(\alpha + k\left|z_1\right|^{1/2}\right)^2}{4\left(\alpha + k\left|z_1\right|^{1/2}\right) - 8} + \dfrac{\delta^2}{4\alpha} \\ k > 0 \end{cases} \tag{12}$$

When the above conditions are satisfied, Eq. (11) can converge to the origin in a certain time.

Letting the perturbation term $e = ((B/J)\omega + (T_L/J)$ and by using variable substitution, the following variables are obtained:

$$\begin{cases} z_1 = s \\ z_2 = -\int \beta \text{sign}\,(z_1)\,\mathrm{d}t + e \end{cases} \tag{13}$$

Derivation of Eq. (13) yields.

$$\begin{cases} \dot{z}_1 = -\alpha |z_1|^{1/2} \text{sign}\,(z_1) - k z_1 + z_2 \\ \dot{z}_2 = -\beta \text{sign}\,(z_1) + \dot{e} \end{cases} \tag{14}$$

In order to verify the stability of the sliding mode speed controller, the Lyapunov function is formulated according to Eq. (11) as follows.

$$V\,(z_1, z_2) = \zeta^T \Pi \zeta \tag{15}$$

where $\zeta^T = [\zeta_1, \zeta_2] = [|z_1|^{1/2}\text{sign}(zl), z_2]$; Π is the real symmetric matrix with the following expressions:

$$\Pi = \begin{bmatrix} 4\beta + \left(\alpha + k\,|z_1|^{1/2}\right)^2 & -\left(\alpha + k\,|z_1|^{1/2}\right) \\ -\left(\alpha + k\,|z_1|^{1/2}\right) & 2 \end{bmatrix} \tag{16}$$

In order to verify the stability of its control system, the derivation of Eq. (15) yields:

$$\dot{V}\,(z_1, z_2) = \dot{\xi}^T \Pi \xi + \xi^T \Pi \dot{\xi} = \frac{1}{2}\frac{1}{|\xi_1|}\left[\xi^T A^T \Pi \xi + \xi^T \Pi A \xi + \rho B^T \Pi \xi + \rho \xi^T \Pi B\right] \tag{17}$$

where $A = \begin{bmatrix} -\left(\alpha + k\,|z_1|^{1/2}\right) & 1 \\ -2\beta & 0 \end{bmatrix}$, $B = \begin{bmatrix} 0 \\ 1 \end{bmatrix}$, $\rho = 2|z_1|^{1/2}$. Obviously, $\rho = 2|z_1|^{1/2}$ is a scalar. Expanding $B^T \Pi \xi$ and $\xi^T \Pi B$ for computational analysis shows that they are both scalars, and $\Pi^T = \Pi$ according to Eq. (16).

So when the conditions $\delta \geqslant 0$ and $2|e| \leqslant \delta$ are satisfied, Eq. (17) can be further reduced to:

$$\begin{aligned} \dot{V}\,(z_1, z_2) &\leq \frac{1}{2}\frac{1}{|\xi_1|}\left[\left(\xi^T A^T \Pi \xi + \xi^T \Pi A \xi + \rho B^T \Pi \xi + \rho \xi^T \Pi B\right) + \delta^2 \xi_1^2 - \rho^2\right] \\ &\leq \frac{1}{2}\frac{1}{|\xi_1|}\left[\xi^T A^T \Pi \xi + \xi^T \Pi A \xi + \delta^2 \xi^T C^T C \xi + \xi^T \Pi B B^T \Pi \xi\right] = -\frac{1}{2}\frac{1}{|\xi_1|}\xi^T Q \xi n \end{aligned} \tag{18}$$

where $Q = -[A^T \Pi + \Pi A + \delta^2 C^T C + \Pi B B^T \Pi]$.

Obviously, Q is a positive definite matrix, so Eq. (18) satisfies the following conditions:

$$\dot{V}\,(z_1, z_2) = -\frac{1}{2}\frac{1}{|\xi_1|}\xi^T Q \xi < 0 \tag{19}$$

From the above analysis, it can be seen that for the system shown in Eq. (11) the corresponding Lyapunov function $V(z_1, z_2)$ satisfies the stability theory of $V > 0$ in the radially unbounded and $\dot{V} < 0$ stability condition.

Further expansion of the positive definite matrix Q yields:

$$Q = \begin{bmatrix} 2\left(\alpha + k\,|z_1|^{\frac{1}{2}}\right)^3 - \left(\alpha + k\,|z_1|^{\frac{1}{2}}\right)^2 + 4\beta\left(\alpha + k\,|z_1|^{\frac{1}{2}}\right) - \delta^2 & 2\left(\alpha + k\,|z_1|^{\frac{1}{2}}\right) - 2\left(\alpha + k\,|z_1|^{\frac{1}{2}}\right)^2 \\ 2\left(\alpha + k\,|z_1|^{\frac{1}{2}}\right) - 2\left(\alpha + k\,|z_1|^{\frac{1}{2}}\right)^2 & 2\left(\alpha + k\,|z_1|^{\frac{1}{2}}\right) - 4 \end{bmatrix} \tag{20}$$

For the system to reach stability, it needs to satisfy $\dot{V} < 0$ stability condition, and according to the above analysis, Q is positive definite. According to the Schur complementary lemma (SCL), for a

real symmetric matrix Q, the parameters of the controller need to satisfy the following conditions since $k > 0$:

$$\begin{cases} \alpha > 0 \\ \beta > \dfrac{\left(\alpha + k\left|z_1\right|^{1/2}\right)^2}{4\left(\alpha + k\left|z_1\right|^{1/2}\right) - 8} + \dfrac{\delta^2}{4\alpha} \\ k > 0 \end{cases} \tag{21}$$

The stability proof of this system is completed. When the above parameters satisfy the above conditions, the output $i_q{}^*$ of the sliding mode speed controller can realize the sliding mode motion and gradually converge to the origin.

3.3. Anti-Disturbance Performance Analysis

The dynamic equation of a permanent magnet synchronous motor can be expressed as follows when the uptake of the internal parameters of the system and the disturbance of the external load is taken into account:

$$\dot{\omega} = \frac{dw}{dt} = \frac{3p_n\psi_f}{2} i_q - \frac{B}{J}\omega - \frac{1}{J}d(t) \tag{22}$$

where $d(t)$ is the total disturbance of the system, including the external load disturbance as well as the internal parameter variations.

Thus, combining Eq. (8), Eq. (10), and Eq. (22), the sliding mode control law is designed as:

$$i_q^* = \frac{2J}{3p_n\psi_f}\left(\left(\frac{B}{J}\omega + \frac{1}{J}d(t)\right) + \alpha|s|^{\frac{1}{2}}\text{sign}(s) + ks + \int \beta\text{sign}(s)\text{d}t\right) \tag{23}$$

It can be seen from Eq. (23) that the dynamic effects of the motor and the control performance of the system are strongly influenced by the uncertainty term $d(t)$. However, in many SMC studies and practical applications, most of them define the perturbation term $d(t)$ as a bounded term and do not observe the perturbation of their systems. Therefore, in this paper an observer is designed as a feedforward to the speed controller. The disturbances of the system are observed in real time and fed back into the controller.

3.4. Sliding Mode Disturbance Observer Design

In order to further improve the anti-interference of the whole system, a sliding mode disturbance observer is designed in this paper. In order to solve the jitter vibration phenomenon existing in the sliding mode observer, a relative improvement is made to the conventional observer. The perturbation observation error is fed back into the switching gain function. The structure is shown in Fig. 1.

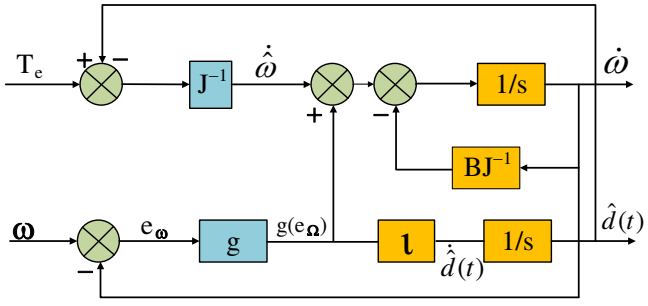

Figure 1. Sliding mode disturbance observer structural diagram.

In a permanent magnet synchronous motor control system with zero first order derivative of load torque disturbance

$$\frac{\text{d}T_L}{\text{d}t} = 0 \tag{24}$$

The first-order derivative of the total system perturbation term $d(t)$ is also zero, as can be seen in Eq. (24):

$$\dot{d}(t) = 0 \tag{25}$$

Set the state variables of the observer to be the total disturbance $d(t)$ of the system and the mechanical angular velocity ω. The input of the system is the electromagnetic torque T_e, and the output is ω. The augmentation matrix of the system is obtained as follows.

$$\begin{bmatrix} \dot{\omega} \\ \dot{d} \end{bmatrix} = \begin{bmatrix} -\dfrac{B}{J} & -\dfrac{1}{J} \\ 0 & 0 \end{bmatrix} \begin{bmatrix} \omega \\ d \end{bmatrix} + \begin{bmatrix} \dfrac{1}{J} \\ 0 \end{bmatrix} T_e \tag{26}$$

The observation object of the sliding mode disturbance observer is set as the total system disturbance $d(t)$, mechanical angular velocity ω, and the observer equation is obtained through Eq. (26) as:

$$\begin{bmatrix} \dot{\hat{\omega}} \\ \dot{\hat{d}} \end{bmatrix} = \begin{bmatrix} -\dfrac{B}{J} & -\dfrac{1}{J} \\ 0 & 0 \end{bmatrix} \begin{bmatrix} \hat{\omega} \\ \hat{d} \end{bmatrix} + \begin{bmatrix} \dfrac{1}{J} \\ 0 \end{bmatrix} T_e + \begin{bmatrix} 1 \\ l \end{bmatrix} g\left(e_\omega\right) \tag{27}$$

where l is the observer gain; $e_\omega = \omega - \hat{\omega}$ is the velocity observation error; and $g(e_\omega)$ is the sliding mode control law.

From Eq. (26) and Eq. (27), the error equation of the sliding mode perturbation observer can be obtained as:

$$\begin{cases} \dot{e}_\omega = -\dfrac{B}{J} e_\omega - \dfrac{1}{J} e_T - g\left(e_\omega\right) \\ \dot{e}_T = -\lg\left(e_\omega\right) \end{cases} \tag{28}$$

where $e_T = d - \hat{d}$ is the perturbation observation error.

The integral sliding surface is selected as follows:

$$s_\omega = e_\omega + c_\omega \int_0^t e_\omega \mathrm{d}t \tag{29}$$

Derivation of s_ω yields:

$$\dot{s}_\omega = \dot{e}_\omega + c_\omega e_\omega \tag{30}$$

The convergence law is chosen as shown in Eq. (31):

$$\dot{s}_\omega = -\varepsilon_\omega \mathrm{sign}\left(s_\omega\right) \tag{31}$$

Combining the $-e_T/J$ operational perturbation term with Eq. (28), Eq. (30), and Eq. (31), the control law of the perturbed observer can be obtained as:

$$g\left(e_\omega\right) = \left(c_\omega - \frac{B}{J}\right) e_\omega + \varepsilon_\omega \mathrm{sign}\left(s_\omega\right) \tag{32}$$

Under the action of the control law of the observer, the trajectory of its system gradually converges to the state origin and reaches the sliding mode surface, from which it follows that:

$$s_\omega = \dot{s}_\omega = 0 \tag{33}$$

$$e_\omega = \dot{e}_\omega \tag{34}$$

From Eq. (34), we have:

$$\begin{cases} e_T = -\mathrm{J}g\left(e_\omega\right) \\ \dot{e}_T = -\lg\left(e_\omega\right) \end{cases} \tag{35}$$

From Eq. (35), we have:

$$e_T = c_T e^{\frac{1}{\zeta}t} \tag{36}$$

where c_T is a constant, and to ensure that e_T can converge to zero in finite time, the parameter l needs to satisfy.

$$l < 0 \tag{37}$$

Then the value of parameter l directly affects the time at which the perturbation observation error converges to zero.

To verify the stability of the sliding mode perturbation observer, the Lyapunov function is defined as follows:

$$V_0 = \frac{1}{2}s_{\omega^2}^2 \tag{38}$$

Derivation of Eq. (38):

$$\dot{V}_o = S_\omega \dot{S}_\omega \tag{39}$$

Combining Eq. (26), Eq. (30), and Eq. (32) yields:

$$\dot{V}_0 = s_\omega \dot{s}_\omega = s_\omega \left(ce_\omega - \frac{B}{J}e_\omega - \frac{1}{J}e_T - g\left(e_\omega\right) \right) = s_\omega \left(-\varepsilon_\omega \text{sign}\left(s_\omega\right) - \frac{e_T}{J} \right) \tag{40}$$

According to the theoretical analysis of the stability of Lyapunov functions, it is known that the sufficient conditions for the existence and accessibility of the slipform surface are:

$$\dot{V}_o = S_\omega \dot{S}_\omega < 0 \tag{41}$$

From Eq. (41), we have:

$$\varepsilon_\omega > \frac{|e_T|}{J} \tag{42}$$

From Eq. (41), it can be seen that the switching gain ε_ω of the observer increases as the load perturbation observation error e_T increases, which leads to a more pronounced dithering of the observations.

$$\varepsilon_\omega = f_\varepsilon \frac{|\varepsilon_T|}{J} \tag{43}$$

where f_ε is constant and $f_\varepsilon > 1$. As e_T tends to zero, ε_ω also tends to zero to weaken the jitter of the observed values. When e_T increases, ε_ω increases accordingly, thus ensuring the robustness of the system.

From the above analysis, it can be seen that the total disturbance term of the system has been fed back to the sliding mode controller in real-time as a known quantity. When there is parameter ingestion and load torque perturbation, the controller can respond to the perturbation change in time, which further improves the system's robustness and effectively improves the response characteristics of the permanent magnet synchronous motor. The system control structure diagram is shown in Fig. 2.

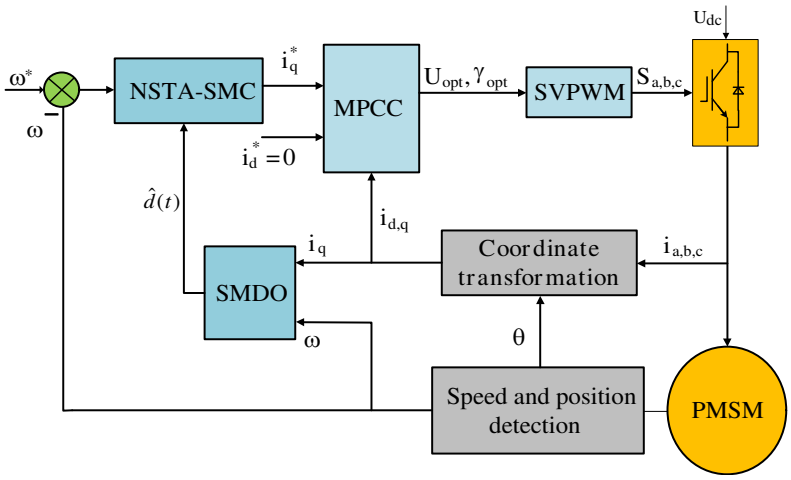

Figure 2. Structure diagram of permanent magnet synchronous motor control system based on NSTA-SMC+SMDO.

4. IMPROVED DUAL VECTOR MPCC

4.1. Voltage Vector Selection and Duty Cycle Optimization

The two-vector current prediction control using optimal duty cycle model predictive current control (MPCC) is shown in Fig. 3.

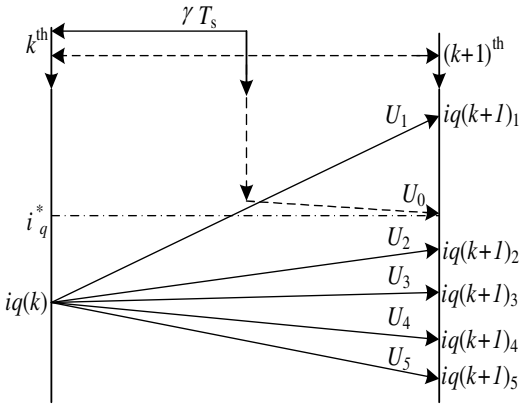

Figure 3. Schematic diagram of optimal voltage vector selection with duty cycle.

In Fig. 3, $i_q(k)$ is the feedback value of the cross-axis current, $i_q(k+1)$ the predicted value of the cross-axis current, and i_q^* the given value of the cross-axis current. In this paper, we choose the principle of no differential beat of the cross-axis current for duty cycle calculation, by allocating the action time of the effective voltage vector and the zero voltage vector in 1 sampling period, so that the cross-axis current reaches the given value at the $(k+1)$th sampling moment.

$$i_q(k+1) = i_q(k) + s_i\gamma_i T_s + s_0\left(T_s - \gamma_i T_s\right) = i_q^* \tag{44}$$

where γ_i is the duty cycle of the optimal voltage vector, and the range is restricted to the interval [0, 1].

From Eq. (19), the duty cycle can be obtained as:

$$\gamma_i = \frac{i_q^* - i_q(k) - s_0 T_s}{T_s\left(s_i - s_0\right)} \tag{45}$$

The optimal duty cycle is calculated in advance for each voltage vector. The value function considers both the voltage vector and the duty cycle when performing optimization, so the optimal voltage vector is optimized as U_1, which ensures the global optimum of the selected voltage vector and can realize the q-axis current without differential beat.

In this paper, when the voltage vector is selected, the first voltage vector is selected in the range of the remaining five effective voltage vectors after removing the effective voltage vector selected in the previous moment, and the second voltage vector is fixed as zero vector following the principle of allowing only one jump in the number of switching times. This can reduce the number of operations per cycle on the one hand and improve the steady-state performance of the system on the other hand.

4.2. Value Function

The control objective of the MPCC strategy is to enable the cross-rectangular current to accurately track the given value of the cross-rectangular current, so the value function is selected in the following form:

$$g_i = \left(i_q^* - i_q(k+1)\right)^2 + \left(i_d^* - i_d(k+1)\right)^2 \tag{46}$$

Considering that the control system introduces many delay problems during operation, such as dead time, delay of inverter output, and filtering, which causes the controller output to lag behind the system current change, $i_q(k+1)$, $i_d(k+1)$ in the value function are replaced by $i_q(k+2)$, $i_d(k+2)$.

4.3. Improved Optimal Duty Cycle MPCC Principle

The improved optimal duty cycle MPCC in the voltage vector selection, the first voltage vector selection range is the remaining five voltage vectors after removing the effective voltage vector selected in the previous moment. This control strategy improves the robustness of the system while reducing the burden of optimal duty cycle calculations. The method system block diagram is shown in Fig. 4 (the effective voltage vector selected in the last cycle U_1 for example).

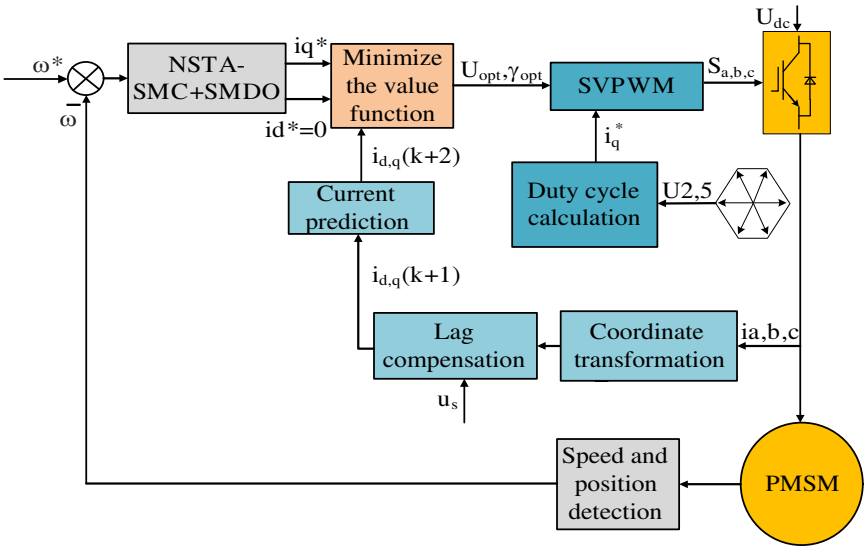

Figure 4. System block diagram of the improved optimal duty cycle MPCC method.

The improved optimal duty cycle MPCC method is as follows:

1) Calculate the duty cycle of each of the five effective voltage vectors according to Eq. (21).
2) According to the PMSM discrete mathematical model Eq. (4) and Eq. (5), the current values of the compensated $i_{d,q}$ under the combination of five voltage vectors and their duty cycles are predicted and substituted into the cost function to calculate the g_i value;
3) The five g_i values are compared, and the voltage vector that minimizes the cost function is selected as the optimal voltage vector. Then the optimal voltage vector and its duty cycle are implemented by the space vector modulation technique.

5. SIMULATION AND EXPERIMENTAL ANALYSIS

In this paper, the proposed current prediction control algorithm is simulated and verified in MATLAB/Simulink software, and an RT-LAB semi-physical control platform based on RT-LAB is built for experiments to compare with the conventional method. The simulated motor parameters are as Table 1.

5.1. Simulation Analysis

The simulation analysis verifies the correctness and effectiveness of the control strategy proposed in this paper, provided that uniform parameters are used throughout the system. The three-speed control strategies, STA-SMC, NSTA-SMC, and NSTA-SMC+SMDO, are analyzed and compared through simulation. The parameters of STA-SMC are: $\alpha = 1500$, $\beta = 60000$, NSTA-SMC: $\alpha = 1500$, $\beta = 60000$, $k = 600$, SMDO: $c_\omega = 2$, $l = -0.8$, $\varepsilon_\omega = 1800$, $f_\varepsilon = 1.5$. The sampling frequency is 10 kHz, and the total simulation time of the system is 0.5 s. Fig. 5 shows the motor speed curve. It shows the speed variation for the three control strategies under different conditions of no-load start, loading, unloading,

Table 1. PMSM parameters for simulation.

Parameters	Value
Permanent magnet chain (Wb)	0.1
Stator inductance (mH)	1.625
Stator resistance (Ω)	0.15
Rated torque (Nm)	15
Rated speed (r/min)	3000
Rated power (W)	200
Rotor inertia ($kg \cdot m^2$)	0.00478
Number of pole pairs	2

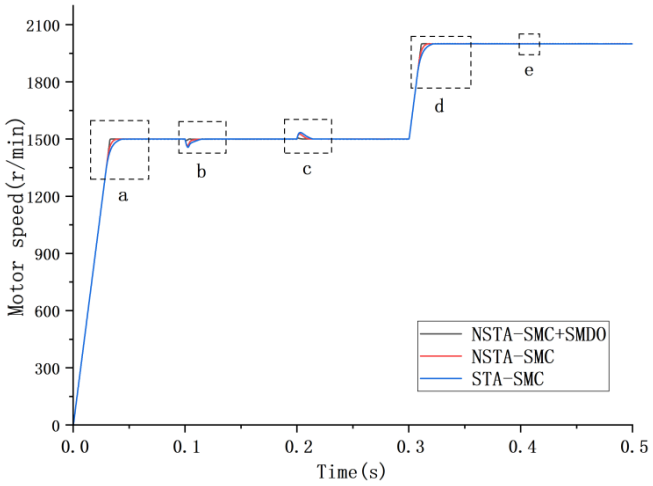

Figure 5. Motor speed curve.

Table 2. Performance comparison of three control strategies.

Result	STA-SMC	NSTA-SMC	NASA-SMC+SMDO
Response time t (s)	0.046	0.040	0.034
Adjustment time t_1 (s)	0.015	0.011	0.005
Adjustment time t_2 (s)	0.022	0.017	0.008
Adjustment time t_3 (s)	0.015	0.012	0.01
Acceleration overshoot (rpm)	0	0	0
Load overshoot (rpm)	43.2	35.0	7.5
Unload overshoot (rpm)	34	26	6.8

and sudden speed changes. When the motor starts at no-load and runs at 1500 (r/min), the analysis from Fig. 6 and Table 2 shows that all three control strategies are free of overshoot. The NSTA-SMC+SMDO control strategy has the shortest response speed and regulation time, 0.012 s faster than the STA-SMC response speed and has the best transient characteristics.

The rated load of 15 Nm is added suddenly at 0.1 s and unloaded at 0.2 s. From the analysis of Fig. 7, Fig. 8, and Table 2, it is clear that the STA-SMC control changes the speed significantly during

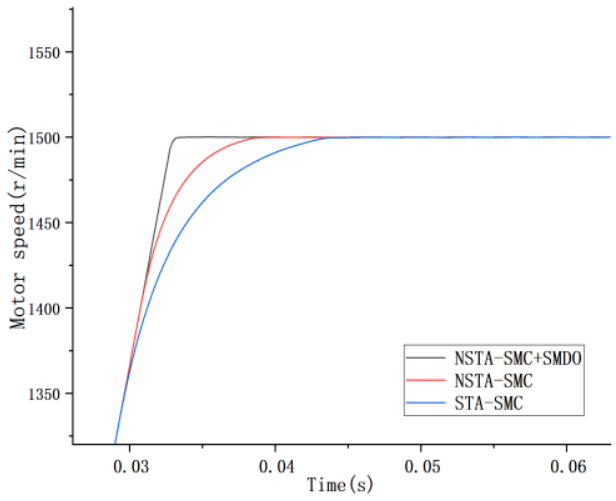

Figure 6. Partial enlarged view of the rotational speed at startup.

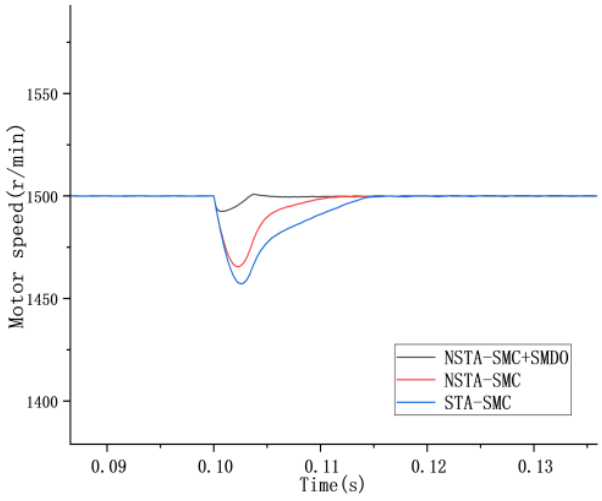

Figure 7. Partial enlarged view of the rotational speed during loading.

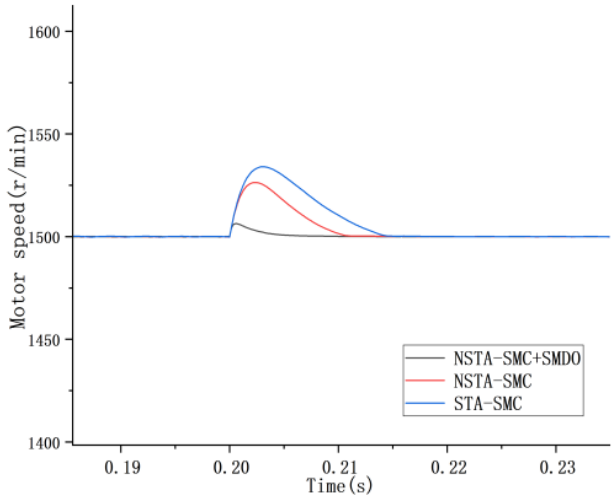

Figure 8. Partial enlarged view of rotational speed during unloading.

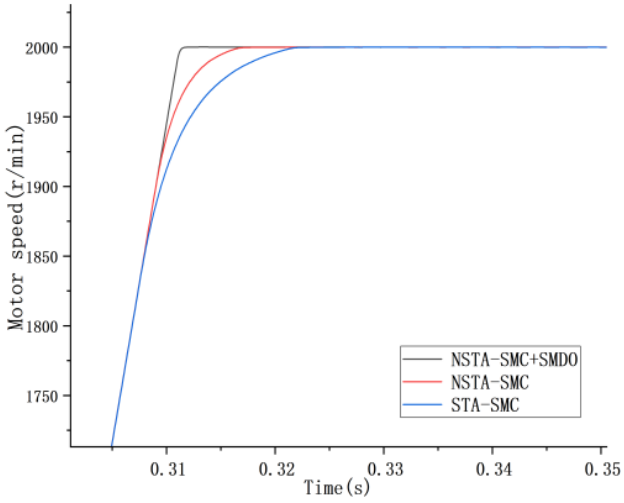

Figure 9. Partial enlarged view of rotational speed during acceleration.

loading and unloading and has the longest regulation time. When a linear term is introduced in the proportional term, NSTA-SMC can make the motor speed converge to the given speed in a shorter time, and the speed change is more minor when the load changes. NSTA-SMC has significantly less regulation time than STA-SMC control in terms of regulation time, with 0.01 s less for the loading process and 0.014 s less for the unloading process. When a sliding mode disturbance observer (SMDO) is combined with NSTA-SMC, its control characteristics improve. Compared with NSTA-SMC, the regulation time is further reduced; the speed variation rate is reduced by 61.2%; and the response characteristics of the whole system are significantly improved.

The speed rises from 1500 (r/min) to 2000 (r/min) at 0.3 s, and the STA-SMC also has the most extended response speed and mediation time in the case of sudden speed change, as shown in the analysis of Fig. 9 and Table 2. When NSTA-SMC+SDMO control is used, the dynamic characteristics are the best, and the speedy response time is the shortest and has good robustness. Compared with STA-SMC, NSTA-SMC effectively weakens the phenomenon of sliding mode jitter. At the same

time, the introduction of SDMO further improves the steady-state characteristics and anti-disturbance characteristics of the control system.

As can be seen in Fig. 10, when the speed is stable at 2000 (r/min), the steady-state error of the STA-SMC and NSTA-SMC speed is the largest, and the control quality is poor. The NSTA-SMC+SMDO, on the other hand, improves the response speed and anti-interference capability of the system without increasing the system jitter. The conflict between the arrival speed of the SMC and the system jitter is effectively resolved.

From the analysis of Fig. 11, it can be seen that the proposed control strategy has lower torque fluctuation and the faster torque response speed than other controls. It has the shorter regulation time and good anti-disturbance performance when it is affected by parameter uptake and load torque disturbance.

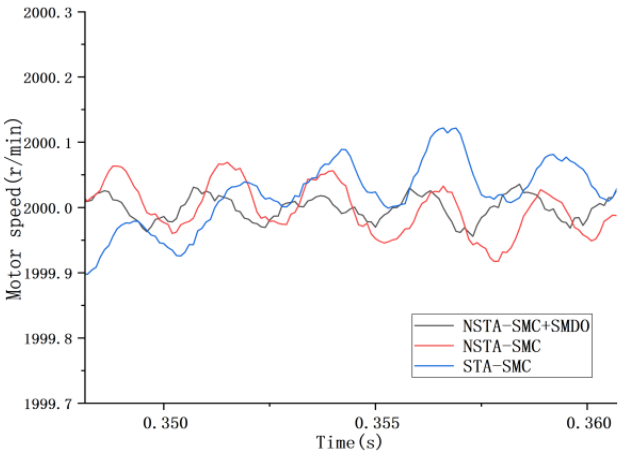

Figure 10. Partial enlarged view of rotational speed at steady state.

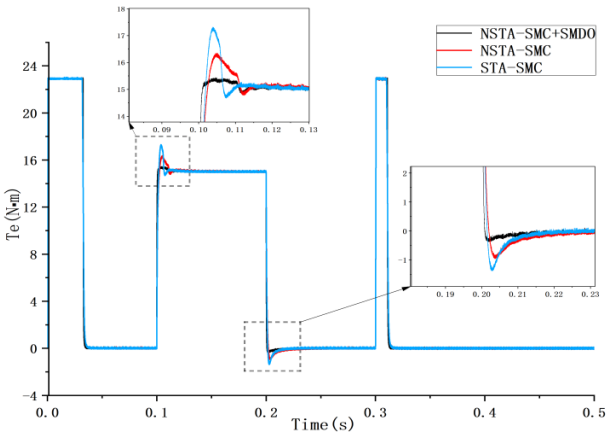

Figure 11. Motor torque change diagram.

5.2. Experimental Analysis

In order to further verify the effectiveness and correctness of the control method proposed in this paper, the RT-LAB experimental platform was built.

The RT-LAB experimental platform consists of the following devices: a DSP controller, an RT-LAB simulation motor, an upper computer, and a scope. The RT-LAB experimental platform is shown in Fig. 12. The parameters of the PMSM are shown in Table 3.

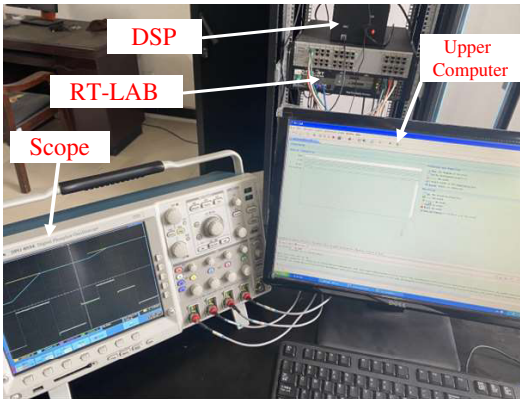

Figure 12. RT-LAB experiment platform.

Table 3. PMSM parameters for the experiment.

Parameters	Value
Permanent magnet chain (Wb)	0.3
Stator inductance (mH)	8.5
Stator resistance (Ω)	2.875
Rated speed (r/min)	1000
Rated power (kw)	1.0
Rated voltage (v)	380
Rotor inertia ($kg \cdot m^2$)	0.00816
Number of pole pairs	4

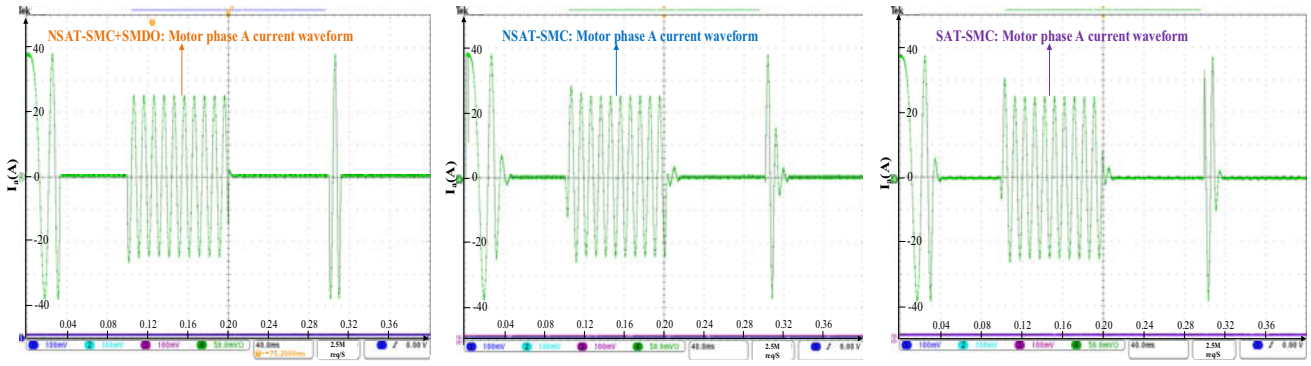

Figure 13. Experimental waveforms of motor phase A current of three control strategies.

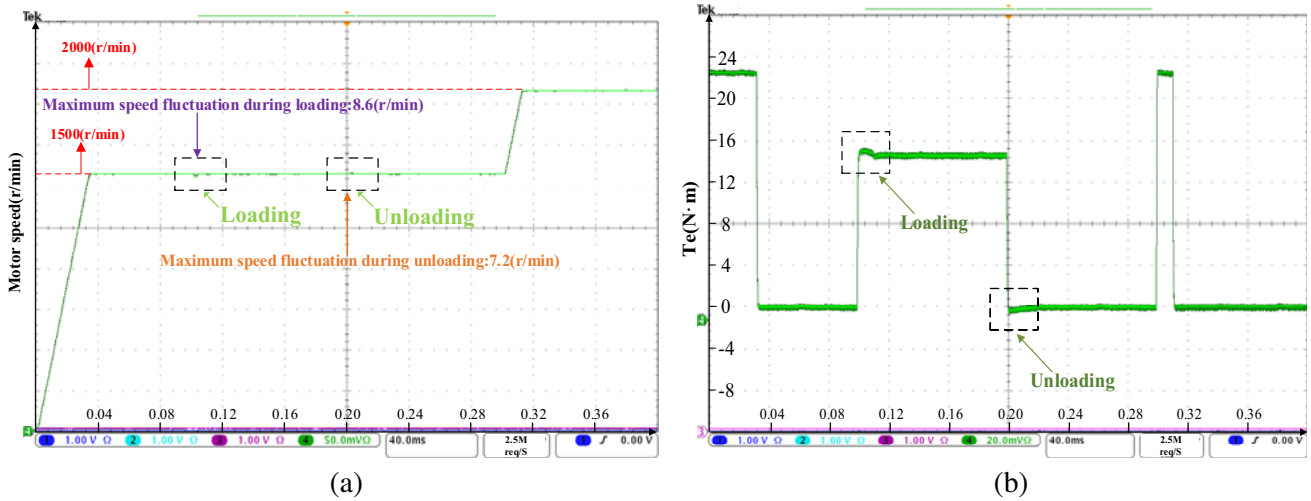

Figure 14. NSTA-SMC+SMDO control. (a) Speed response curve during load changes. (b) Torque response curve during load changes.

Figures 13, 14, 15, and 16 show the experimental results of three control strategies, NSTA-SMC+SMDO, NSTA-SMC, and STA-SMC. The following results can be obtained by analyzing the processes of start-up, acceleration, loading, and unloading.

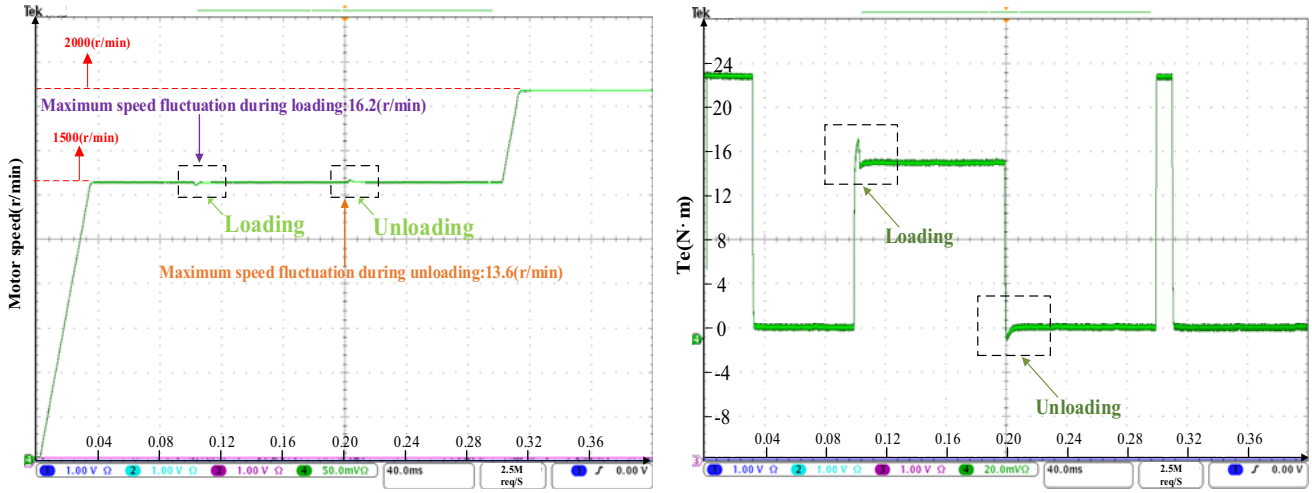

Figure 15. NSTA-SMC control. (a) Speed response curve during load changes. (b) Torque response curve during load changes.

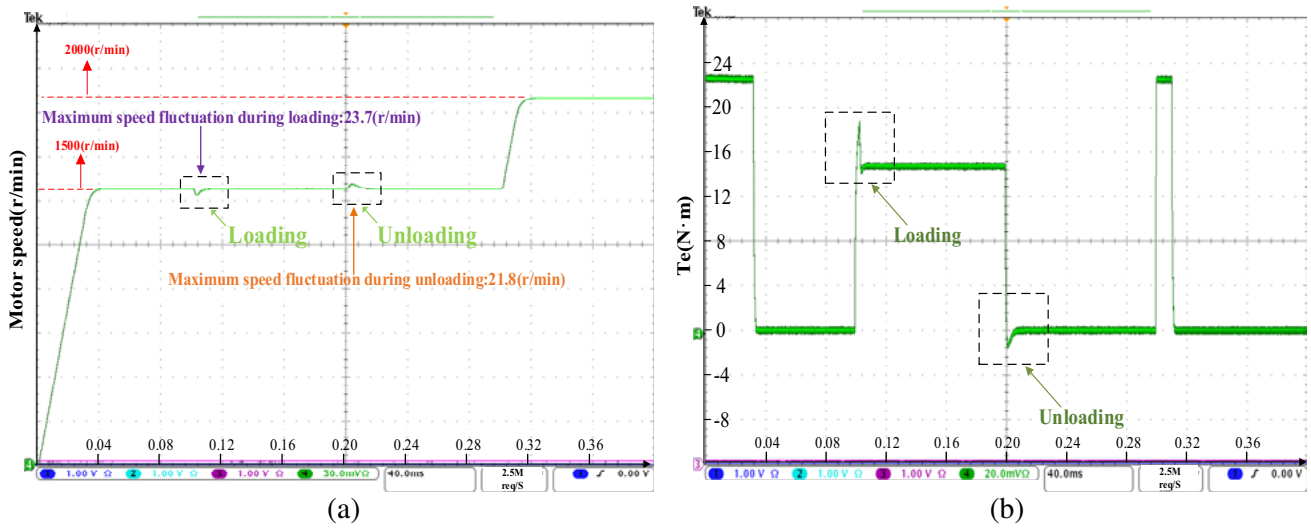

Figure 16. STA-SMC control. (a) Speed response curve during load changes. (b) Torque response curve during load changes.

Figure 13 shows the three control strategies' A-phase output waveforms during motor loading, unloading, and acceleration. The fundamental frequency of the motor is 100 Hz. When the loading and unloading are stable, it can be seen from the analysis in Fig. 13 that when the NSTA-SMC+SMDO control strategy is used, the current harmonics are 5.22%, the current harmonics of NSTA-SMC 11.96%, and STA-SMC 15.68%. From the FFT analysis, it can be seen that the control strategy proposed in this paper reduces: 56.35% and 66.71%, respectively compared to the other two strategies. The improved control strategy effectively reduces the higher harmonic components of the current, mainly the third harmonic and fifth harmonic.

When the motor is unloaded, the speed response curve analysis shows that the NSTA-SMC+SMDO has faster start-up response and shorter regulation time than the STA-SMC and NSTA-SMC, and its steady-state error is the smallest when the speed reaches steady state. The steady-state error of STA-SMC is: 0.046 (r/min), NSTA-SMC: 0.038 (r/min), and NSTA-SMC+SMDO is the smallest with the

value of 0.029 (r/min). When the speed rises from 1500 (r/min) to 2000 (r/min), STA-SMC has the longest response speed and mediation time. When NSTA-SMC+SDMO control is used, the best dynamic characteristics, the shortest speed response time, and good robustness are achieved.

When the load is changed, a disturbance of 15 Nm is added at 0.1 s, and a disturbance of 15 Nm is removed at 0.2 s. The analysis of the experimental results shows that the maximum speed fluctuation value of STA-SMC is: 23.7 (r/min); the maximum speed fluctuation of NSTA-SMC is: 16.2 (r/min); the NSTA-SMC+SMDO is reduced to 8.6 (r/min), and its speed regulation time is the shortest. The analysis of the torque response curve shows that NSTA-SMC+SMDO has faster torque response and smaller overshoot than the other two controls.

The analysis of the above experimental results shows that the control characteristics of the whole system are effectively improved by introducing the linear term into the proportional term. In combination with the sliding mode disturbance observer, the disturbance of the system can be estimated in real-time as a feedforward. Sliding mode jitter is suppressed while the system robustness is further improved.

6. CONCLUSION

From the analysis of simulation and experimental results, the NSTA-SMC+SMDO control strategy proposed in this paper has better anti-disturbance characteristics. That is, it can weaken the jitter and also effectively improve the robustness and control performance of the system.

(1) The results of simulations and experiments show that when the linear term is introduced into the proportional term, the NSTA-SMC control strategy solves the problems of poor anti-disturbance and slow speed caused by the square root calculation in the original algorithm. Compared with the STA-SMC control, the NSTA-SMC has a faster response and good steady-state characteristics.

(2) The switching gain in the SMDO designed in this paper is a function related to the perturbation observation error. This function can effectively suppress the jitter of the sliding mode observer and improve its performance. The simulated and experimental results show that the NSTA-SMC+SMDO control strategy proposed in this paper can further improve the control system's response speed and anti-disturbance capability.

ACKNOWLEDGMENT

This work was supported by the National Natural Science Foundation of China under Grant Number 51907061, and Educational Commission of Hunan Province of China under Grant Number 21B0552.

REFERENCES

1. Tong, W., S. Dai, S. Wu, and R. Tang, "Performance comparison between an amorphous metal PMSM and a silicon steel PMSM," *IEEE Transactions on Magnetics*, Vol. 55, No. 6, 1–5, Art No. 8102705, Jun. 2019, doi: 10.1109/TMAG.2019.2900531.
2. Ding, X., J. Cheng, Z. Zhao, and P. Chi Kwong Luk, "A high-precision and high-efficiency PMSM driver based on power amplifiers and RTSPSs," *IEEE Transactions on Power Electronics*, Vol. 36, No. 9, 10470–10480, Sept. 2021, doi: 10.1109/TPEL.2021.3063312.
3. Zhang, Y. and H. Yang, "Model predictive torque control of induction motor drives with optimal duty cycle control," *IEEE Transactions on Power Electronics*, Vol. 29, No. 12, 6593–6603, Dec. 2014, doi: 10.1109/TPEL.2014.2302838.
4. Song, Z., Y. Tian, W. Chen, Z. Zou, and Z. Chen, "Predictive duty cycle control of three-phase active-front-end rectifiers," *IEEE Transactions on Power Electronics*, Vol. 31, No. 1, 698–710, Jan. 2016, doi: 10.1109/TPEL.2015.2398872.
5. Yan, Y., S. Wang, C. Xia, H. Wang, and T. Shi, "Hybrid control set-model predictive control for field-oriented control of VSI-PMSM," *IEEE Transactions on Energy Conversion*, Vol. 31, No. 4, 1622–1633, Dec. 2016, doi: 10.1109/TEC.2016.2598154.

6. Sheng, L., W. Li, Y. Wang, M. Fan, and X. Yang, "Sensorless control of a shearer short-range cutting interior permanent magnet synchronous motor based on a new sliding mode observer," *IEEE Access*, Vol. 5, 18439–18450, 2017, doi: 10.1109/ACCESS.2017.2734699.
7. Ji, Z. C. and J. Chang, "Speed-sensorless control of PMSM based on an improved equivalent input disturbance estimator," *Chin. J. Sci. Instrum.*, Vol. 30, No. 10, 2139–2143, Oct. 2009.
8. Zhou, X. Y., L. L. Li, and L. B. Zhao, "Nonsingular terminal sliding mode control for the ESO-based stabilized platform," *Chin. J. Sci. Instrum.*, Vol. 39, No. 5, 161–169, May 2018.
9. Cao, Z. and F. Meng, "Adaptive observer-based inverse optimal control of a class of second-order Euler-Lagrange systems," *2021 IEEE 7th International Conference on Cloud Computing and Intelligent Systems (CCIS)*, 300–304, 2021, doi: 10.1109/CCIS53392.2021.9754605.
10. Ma, Z. and S. M. Jiao, "Research on the attitude control of quad-rotor UAV based on active disturbance rejection control," *2017 3rd IEEE International Conference on Control Science and Systems Engineering (ICCSSE)*, 45–49, 2017, doi: 10.1109/CCSSE.2017.8087892.
11. Wu, J., et al., "A ditherless bias control technique for IQ Mach-Zehnder modulator based on partial derivative and neural network," *2021 Asia Communications and Photonics Conference (ACP)*, 1–3, 2021.
12. Zhang, Q. and S. Zhang, "Sliding mode control based on disturbance compensation reaching law for pressure difference in cement mill," *2021 China Automation Congress (CAC)*, 771–775, 2021, doi: 10.1109/CAC53003.2021.9727546.
13. Anuar, H. A., F. Plestan, A. Chriette, and O. Kermorgant, "Sliding mode control with adaptive gain of quadrotor with rigid manipulator," *2021 20th International Conference on Advanced Robotics (ICAR)*, 547–554, 2021, doi: 10.1109/ICAR53236.2021.9659433.
14. Ji, P., F. Ma, and F. Min, "Terminal traction control of teleoperation manipulator with random jitter disturbance based on active disturbance rejection sliding mode control," *IEEE Access*, Vol. 8, 220246–220262, 2020, doi: 10.1109/ACCESS.2020.3043247.
15. Levant, A., "Principles of 2-sliding mode design," *Automatica*, Vol. 43, No. 4, 576–586, 2007.
16. Zhang, L., J. Bai, and J. Wu, "SPMSM sliding mode control based on the new super twisting algorithm," *Complexity*, Vol. 2021, Article ID 2886789, 9 pages, 2021.
17. Hou, Q., S. Ding, and X. Yu, "Composite super-twisting sliding mode control design for PMSM speed regulation problem based on a novel disturbance observer," *IEEE Transactions on Energy Conversion*, Vol. 36, No. 4, 2591–2599, Dec. 2021, doi: 10.1109/TEC.2020.2985054.
18. Qu, L., W. Qiao, and L. Qu, "An extended-state-observer-based sliding-mode speed control for permanent-magnet synchronous motors," *IEEE Journal of Emerging and Selected Topics in Power Electronics*, Vol. 9, No. 2, 1605–1613, Apr. 2021, doi: 10.1109/JESTPE.2020.2990442.
19. Qin, J., Q. Ma, H. Gao, and W. X. Zheng, "Fault-tolerant cooperative tracking control via integral sliding mode control technique," *IEEE/ASME Transactions on Mechatronics*, Vol. 23, No. 1, 342–351, Feb. 2018, doi: 10.1109/TMECH.2017.2775447.
20. Li, Z., S. Zhou, Y. Xiao, and L. Wang, "Sensorless vector control of permanent magnet synchronous linear motor based on self-adaptive super-twisting sliding mode controller," *IEEE Access*, Vol. 7, 44998–45011, 2019, doi: 10.1109/ACCESS.2019.2909308.
21. Hou, Q., S. Ding, X. Yu, and K. Mei, "A super-twisting-like fractional controller for SPMSM drive system," *IEEE Transactions on Industrial Electronics*, Vol. 69, No. 9, 9376–9384, Sept. 2022, doi: 10.1109/TIE.2021.3116585.
22. Junejo, A. K., W. Xu, C. Mu, M. M. Ismail, and Y. Liu, "Adaptive speed control of PMSM drive system based a new sliding-mode reaching law," *IEEE Transactions on Power Electronics*, Vol. 35, No. 11, 12110–12121, Nov. 2020, doi: 10.1109/TPEL.2020.2986893.
23. Hou, Q. and S. Ding, "GPIO based super-twisting sliding mode control for PMSM," *IEEE Transactions on Circuits and Systems II: Express Briefs*, Vol. 68, No. 2, 747–751, Feb. 2021, doi: 10.1109/TCSII.2020.3008188.

24. Liu, W., S. Chen, and H. Huang, "Adaptive nonsingular fast terminal sliding mode control for permanent magnet synchronous motor based on disturbance observer," *IEEE Access*, Vol. 7, 153791–153798, 2019, doi: 10.1109/ACCESS.2019.2948945.
25. Li, W., Z. Du, W. Wang, and W. Wu, "Composite fractional order sliding mode control of permanent magnet synchronous motor based on disturbance observer," *2019 Chinese Automation Congress (CAC)*, 4012–4016, 2019, doi: 10.1109/CAC48633.2019.8996422.
26. Zhang, L., S. Wang, and J. Bai, "Fast-super-twisting sliding mode speed loop control of permanent magnet synchronous motor based on SVM-DTC," *IEICE Electronics Express*, Vol. 18, 1, 2020.
27. Wang, Y., et al., "Deadbeat model-predictive torque control with discrete space-vector modulation for PMSM drives," *IEEE Transactions on Industrial Electronics*, Vol. 64, No. 5, 3537–3547, May 2017, doi: 10.1109/TIE.2017.2652338.